

# Three-Step Conditional Diffusion 3D Reconstruction for Light-Field Microscopy\*

Qihong Zhao<sup>1</sup> Shaokang Yan<sup>1</sup> Zhimin Qiao<sup>1</sup> Jinjia Wang<sup>1†</sup> Bo Xiong<sup>2\*</sup>

<sup>1</sup>Yanshan University <sup>2</sup>Peking University

{zhaoqh, yskjy, qzm}@stumail.yzu.edu.cn wjj@ysu.edu.cn xiongbo@pku.edu.cn

## Abstract

Light-field microscopy (LFM) enables single-shot capture of multi-angular information from biological samples, supporting real-time volumetric imaging. However, traditional physics-based algorithms often suffer from limited spatial resolution, severe artifacts, and high computational costs. Existing learning-based methods improve inference efficiency but still face limitations in reconstruction accuracy and generalization capability. To address these challenges, this paper proposes a high-fidelity Three-Step Conditional Diffusion (TCD) 3D reconstruction method for LFM. Although conventional diffusion models have achieved remarkable success in generative modeling, their slow sampling process and the inherent trade-off between quality and efficiency hinder their application in real-time 3D imaging. We redesign the diffusion process through a deterministic three-step sampling strategy coupled with a lightweight conditional U-Net, establishing a new paradigm for fast and accurate volumetric reconstruction. Furthermore, an Inter-Class Detection (ICD) module is incorporated to identify out-of-distribution or anomalous inputs during inference, thereby enhancing model stability and reliability. Extensive experiments and cross-dataset evaluations demonstrate that TCD significantly outperforms state-of-the-art methods in both reconstruction fidelity and generalization, providing an efficient and practical 3D reconstruction solution for light-field microscopy.

## 1. Introduction

Light-field microscopy (LFM) has emerged as a promising technique for 3D imaging. It enables instantaneous volumetric reconstruction of living specimens and offers unique advantages in capturing dynamic biological processes. These properties make LFM particularly suitable for time-sensitive biological studies [24, 40, 46], such as neural activity imaging, embryonic development monitoring, and cellular dynamics observation [8, 42].

\*Accepted to CVPR 2026 Findings.

†Corresponding authors.

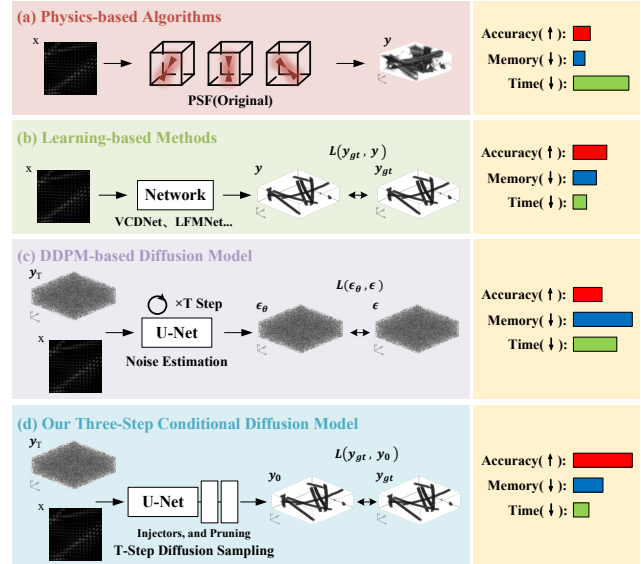


Figure 1. **Comparison of our TCD model with representative imaging methods:** (a) **Physics-based algorithms:** Based on wave optics, these methods reconstruct 3D volumes by utilizing the system’s point spread function (PSF) matrix. (b) **Learning-based methods:** Deep neural networks employ supervised learning to map light-field images to 3D volumes. (c) **DDPM-based diffusion model:** This method trains a U-Net-based one-step noise estimator and performs iterative sampling over hundreds of steps using the predicted noise. (d) **Our improved diffusion model:** This method employs an end-to-end architecture and injects conditional priors into the pruned noise estimation U-Net.

Traditional reconstruction algorithms based on wave-optics models rely heavily on accurate optical modeling and complex iterative optimization. Despite their strong physical interpretability [3, 29], these physics-driven methods often struggle to handle real-world noise and complex biological structures under static priors, resulting in limited spatial resolution, severe reconstruction artifacts, and high computational cost [36, 37].

The rapid progress of deep learning has led to the introduction of neural networks in LFM reconstruction. These networks learn the complex nonlinear mapping from light-

field images to 3D volumes, achieving notable improvements in both speed and reconstruction quality [17]. Nevertheless, their generalization capability remains limited [44], which hinders stable performance across diverse experimental conditions and specimen types.

The Denoising Diffusion Probabilistic Model (DDPM), based on Markov chains, has demonstrated exceptional generative capabilities by progressively synthesizing high-fidelity structures [12]. However, its high computational burden and slow inference limit real-time applications in 3D imaging [16]. To overcome these limitations, we propose a Three-Step Conditional Diffusion (TCD) model for efficient and high-quality light-field 3D reconstruction. Inspired by the deterministic DDIM sampling strategy [4, 19], the reverse diffusion process is compressed into just three steps (a number determined experimentally in our framework), achieving an effective trade-off between efficiency and reconstruction quality. Furthermore, the U-Net backbone is redesigned with physics-guided conditional priors injected at each layer and pruned into a compact three-stage architecture, substantially reducing model complexity while preserving reconstruction accuracy.

In addition, we introduce an Inter-Class Detection (ICD) module to evaluate whether a test sample falls within the training distribution. For out-of-distribution (OOD) samples, the system supports rapid fine-tuning with newly collected data to ensure high-quality reconstruction. This mechanism further enhances the model’s generalization and robustness across diverse biological specimens [11], guaranteeing stable and reliable performance under varying experimental conditions.

A comparison of representative 3D reconstruction methods for LFM is shown in Figure 1. The main characteristics and contributions of this work are summarized as follows:

- **Efficient diffusion model for LFM:** We are the first to introduce a diffusion-based framework into 3D reconstruction for LFM, employing a deterministic sampling strategy that compresses the generation process from hundreds of iterations to only three, greatly accelerating inference.
- **End-to-end volume prediction:** We reformulate the traditional noise-prediction objective into a direct volume reconstruction paradigm, improving both representational capability and training stability.
- **Light-field guidance and network pruning:** We inject light-field conditional priors and simplify the network structure to reduce model size while preserving reconstruction accuracy.
- **Integration of Inter-Class Detection:** We propose an ICD module that adaptively assesses data distributions to detect out-of-distribution samples and enhance the model’s generalization and robustness across diverse biological specimens.

Experimental results on multiple LFM datasets demonstrate that our method achieves superior reconstruction fidelity and strong generalization capability, thus verifying the potential and effectiveness of diffusion models for 3D imaging in biological microscopy.

## 2. Related Work

### 2.1. Physics-based 3D reconstruction method

Traditional confocal fluorescence microscopy relies on sequential scanning to acquire volumetric slices, resulting in long exposure times, photobleaching, and phototoxicity, which limit its application in live-cell dynamic imaging [1, 28]. To overcome these constraints, Levoy et al. introduced a microlens array (MLA) into a conventional microscope, pioneering the structure of light-field microscopy and enabling four-dimensional light-field data acquisition [14, 15]. With its scan-free and high-speed imaging advantages, LFM has been widely applied to real-time volumetric imaging of dynamic biological processes. However, at the microscopic scale, highly transparent specimens cause complex light scattering [2, 14, 29], making ray-optics-based models insufficient for accurately describing light propagation and imposing inherent limits on spatial resolution [5, 23].

Broxton et al. proposed Richardson–Lucy deconvolution (RLD), a wave-optics-based iterative approach that significantly enhances spatial resolution compared to earlier ray-optics-based models [3, 7, 34]. Subsequent studies introduced frequency-domain deconvolution and phase-space deconvolution in the angular-frequency domain [20, 32, 33], both of which improved reconstruction quality and convergence speed. Herman et al. incorporated sparse priors within an alternating direction method of multipliers (ADMM) framework [36, 37], while Zhao et al. applied sparse deconvolution to accelerate convergence, suppress noise-induced artifacts, and improve spatial resolution [45]. Although these methods achieve partial super-resolution, their reliance on sparse priors limits generalizability across diverse microscopic samples.

### 2.2. Learning-based 3D reconstruction method

With the advent of deep learning, convolutional neural networks (CNNs) have been applied to 3D reconstruction for LFM. In 2021, Wang et al. proposed a view-channel-depth network [39], achieving high-resolution 3D reconstruction at video frame rates and laying the foundation for subsequent learning-based LFM methods. Subsequent studies introduced advanced architectures, including the 4D convolution-based LFMNet [38], the implicit neural representation network DINER [47], and CWFA, which employs invertible normalizing flows with limited training data [22]. Although these learning-based approaches have achieved

significant improvements in reconstruction accuracy and efficiency, they still face challenges in generalization and interpretability [44].

In recent years, diffusion models have demonstrated remarkable generative capabilities across images, volumes, and videos [6, 9]. Unlike conventional CNNs that directly map inputs to outputs, diffusion models learn data distributions by estimating noise, enabling them to capture complex spatial structures and fine-grained details. Their iterative denoising process enhances robustness and generalization, while the forward–reverse diffusion can be formulated as a Markov chain, providing physical interpretability [19]. By incorporating conditional information as guidance [10], conditional diffusion models achieve controllable and semantically consistent generation [21, 43]. For instance, in text-to-image diffusion [25, 27], textual conditioning enables fine-grained control over spatial and semantic attributes, resulting in high-resolution, realistic outputs. Motivated by these properties, diffusion models offer a theoretical foundation for high-fidelity, controllable, and interpretable reconstruction in complex tasks such as 3D reconstruction for LFM [21, 26].

### 2.3. Inter-Class Detection for LFM

In high-fidelity LFM 3D reconstruction, distributional variations in input samples challenge model generalization, particularly when encountering novel biological specimens and experimental conditions. To address this issue, inter-class detection modules have been proposed to estimate the distributional confidence of input data. Early out-of-distribution detection methods mainly relied on simple confidence metrics or softmax outputs [13]. However, these approaches often perform unstably in complex, high-dimensional microscopy data. Subsequently, methods based on feature-space distances or generative models were developed to more accurately determine whether a sample belongs to the training distribution. For instance, ODIN [18] enhances OOD recognition using temperature scaling and input perturbations, while the Mahalanobis distance-based approach [41] estimates inter-class confidence from feature distribution statistics. Although these methods achieve notable performance in general computer vision tasks, their direct application to LFM reconstruction remains challenging due to the high dimensionality of input light-field data and complex optical conditions [35].

## 3. Method

In this section, we first introduce the traditional DDPM framework applied to 3D reconstruction for LFM. Next, we describe TCD based on this framework, with a detailed presentation of its core design components. Finally, we present the ICD module, forming the complete reconstruction pipeline.

### 3.1. Preliminaries: Diffusion Models

Our framework is grounded in the DDPM paradigm, which formulates data generation as a gradual denoising process driven by a Markov chain. Specifically, the modeling framework integrates thermodynamic diffusion theory with deep learning-based probabilistic inference [30], leveraging the physical interpretability of diffusion processes and the representational power of neural networks. It consists of two main stages: a forward diffusion process and a reverse denoising process. To adapt the DDPM for LFM 3D reconstruction, we integrate light-field images and noisy volumes as inputs, enabling effective data fusion for volumetric reconstruction.

#### 3.1.1. Forward Diffusion

Given a clean 3D volume  $\mathbf{y}_0 \in \mathbb{R}^{D \times H \times W}$ , Gaussian noise is gradually added through a Markov process over  $T$  timesteps to generate a pure noise volume  $\mathbf{y}_T$ . At each timestep  $t$ , the process is defined as:

$$\mathbf{y}_t = \sqrt{\alpha_t} \mathbf{y}_{t-1} + \sqrt{1 - \alpha_t} \cdot \epsilon, \quad (1)$$

where  $\epsilon \sim \mathcal{N}(0, \mathbf{I})$  is standard Gaussian noise,  $\mathbf{y}_t$  denotes the noisy volume at timestep  $t$ , and  $\alpha_t = 1 - \beta_t$  with the noise schedule  $\beta_t \in [0, 1]$ ,  $\beta_0 = 0$ .

According to the variance-preserving stochastic differential equation (VP-SDE) [31], the noisy volume  $\mathbf{y}_t$  can also be directly computed from the original clean volume  $\mathbf{y}_0$  as:

$$\mathbf{y}_t = \sqrt{\bar{\alpha}_t} \mathbf{y}_0 + \sqrt{1 - \bar{\alpha}_t} \cdot \epsilon, \quad (2)$$

where  $\bar{\alpha}_t = \prod_{i=1}^t \alpha_i$  is the cumulative product of  $\alpha_i$ .

During training, a random timestep  $t \sim \mathcal{U}(0, T)$  is selected. The noisy volume  $\mathbf{y}_t$ , the corresponding conditional light-field image  $\mathbf{x}$ , and the timestep  $t$  are fed into a U-Net-based noise prediction network  $\epsilon_\theta$  (where  $\theta$  denotes the trainable parameters of the diffusion network). The model is optimized by minimizing the mean squared error (MSE) between the true noise  $\epsilon$  and the predicted noise  $\epsilon_\theta$ :

$$\arg \min_{\theta} \left\| \epsilon - \epsilon_\theta \left( \sqrt{\bar{\alpha}_t} \mathbf{y}_0 + \sqrt{1 - \bar{\alpha}_t} \cdot \epsilon, \mathbf{x}, t \right) \right\|_2^2. \quad (3)$$

#### 3.1.2. Reverse Denoising

To recover the clean 3D volume, we adapt the reverse diffusion process, which iteratively approximates the posterior distribution  $p_\theta(\mathbf{y}_{t-1} | \mathbf{y}_t)$  based on Bayes’ theorem and Gaussian combination rules [12]:

$$p_\theta(\mathbf{y}_{t-1} | \mathbf{y}_t) = \mathcal{N}(\mathbf{y}_{t-1}; \mu_\theta(\mathbf{y}_t, \mathbf{x}, t), \sigma_t^2 \mathbf{I}), \quad (4)$$

where  $\mu_\theta(\mathbf{y}_t, \mathbf{x}, t)$  and  $\sigma_t$  denote the predicted mean and the sampling variance, respectively, at each timestep  $t$ .

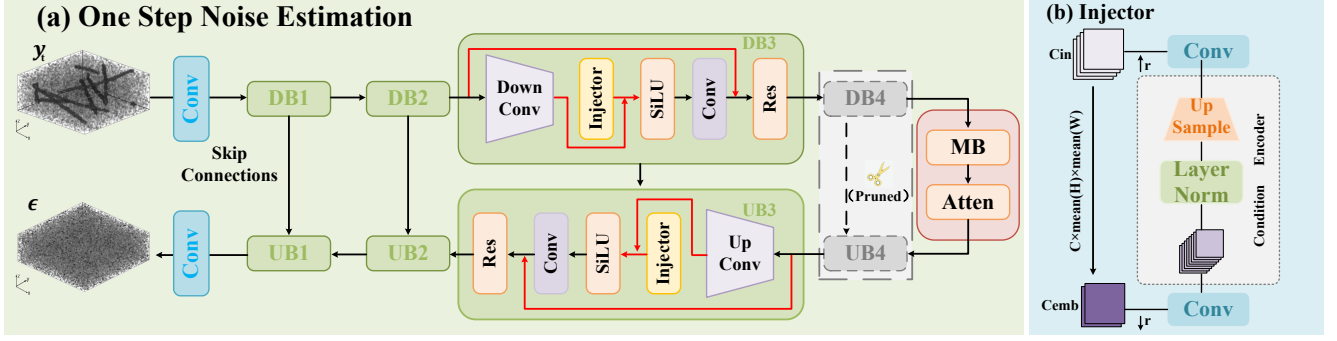


Figure 2. **Overview of the U-Net-based one-step noise estimation framework.** (a) The main U-Net architecture, composed of a sequence of Downsampling Blocks (DBs), Upsampling Blocks (UBs), and a Middle Block (MB) that includes a self-attention (Atten) module. Injectors are integrated within these blocks to enhance reconstruction fidelity. To reduce model complexity, select blocks are pruned. (b) The Injector module. This module is designed to fuse the prior guidance provided by the light-field input  $C_{in}$ . It uses a specific network structure combined with residual connections to inject physics information into the Sampling Blocks of the U-Net.

Instead of modeling the full data distribution, our network learns to predict the noise, enabling the following update rule:

$$\mathbf{y}_{t-1} = \frac{1}{\sqrt{\alpha_t}} \left( \mathbf{y}_t - \frac{\beta_t}{\sqrt{1-\bar{\alpha}_t}} \cdot \epsilon_\theta(\mathbf{y}_t, \mathbf{x}, t) \right) + \sigma_t \cdot \epsilon_{\text{rand}}, \quad (5)$$

where  $\epsilon_\theta(\mathbf{y}_t, \mathbf{x}, t)$  is the predicted noise at step  $t$ , and  $\epsilon_{\text{rand}} \sim \mathcal{N}(0, \mathbf{I})$  is a randomly sampled Gaussian noise introduced to maintain diversity.

This denoising process proceeds in reverse from  $t = T$  to  $t = 0$ , gradually removing the accumulated noise and producing the final clean volume  $\mathbf{y}_0$  conditioned on the light-field measurement  $\mathbf{x}$ . A visualization of the DDPM denoising process over 500 steps is provided in the supplementary material.

### 3.2. Three-Step Conditional Diffusion

To address the inefficiency and stochasticity of conventional DDPMs, we propose a deterministic Three-Step Conditional Diffusion framework for LFM 3D reconstruction. TCD achieves high-fidelity reconstruction while significantly accelerating inference through a three-step deterministic sampling strategy. By integrating an end-to-end optimized, physics-guided lightweight U-Net, our framework effectively balances reconstruction quality and computational cost.

#### 3.2.1. Deterministic Sampling Strategy (T=3)

Standard DDPM inference requires hundreds of reverse denoising steps, resulting in high computational cost and slow inference speed. To improve efficiency, we adopt a DDIM-inspired deterministic sampling strategy, which replaces stochastic noise sampling with a deterministic update process using fixed timesteps, thereby significantly accelerating the inference process.

During denoising, the noise predictor  $\epsilon_\theta$  guides the denoising direction. The deterministic sampling involves two key steps:

$$\mathbf{y}_{0|t} = \frac{1}{\sqrt{\bar{\alpha}_t}} \left( \mathbf{y}_t - \sqrt{1-\bar{\alpha}_t} \cdot \epsilon_\theta(\mathbf{y}_t, \mathbf{x}, t) \right), \quad (6)$$

$$\mathbf{y}_{t-1} = \sqrt{\bar{\alpha}_{t-1}} \cdot \mathbf{y}_{0|t} + \sqrt{1-\bar{\alpha}_{t-1}} \cdot \epsilon_\theta(\mathbf{y}_t, \mathbf{x}, t).$$

This process can be equivalently combined as:

$$\mathbf{y}_{t-1} = \sqrt{\bar{\alpha}_{t-1}} \left( \frac{\mathbf{y}_t - \sqrt{1-\bar{\alpha}_t} \cdot \epsilon_\theta(\mathbf{y}_t, \mathbf{x}, t)}{\sqrt{\bar{\alpha}_t}} \right) + \sqrt{1-\bar{\alpha}_{t-1}} \cdot \epsilon_\theta(\mathbf{y}_t, \mathbf{x}, t). \quad (7)$$

Unlike DDPM and DDIM, our sampling strategy constructs a deterministic equivalent reverse process, bypassing the full Markov chain by reformulating sampling as a 3D-optimized unrolled network. This formulation enables high-fidelity inference with significantly fewer steps. Furthermore, flexible timestep scheduling allows for a controllable trade-off between efficiency and quality, catering to real-time 3D reconstruction and generation. As validated in Figure 5, TCD uses only three deterministic steps to achieve over a 90% reduction in sampling cost while maintaining reconstruction accuracy.

#### 3.2.2. End-to-End Reconstruction Network

To enable a direct, end-to-end reconstruction mapping from an initial noise volume to the ground truth 3D volume  $\mathbf{y}_{\text{gt}}$ , we extend the deterministic sampling acceleration strategy into a full sampling network. This network is composed of  $T$  sequentially stacked U-Net modules, formulated as:

$$F = F_1 \circ F_2 \circ \dots \circ F_T, \quad \mathbf{y}_{t-1} = F_t(\mathbf{y}_t, \mathbf{x}, t), \quad (8)$$

where each function  $F_t(\mathbf{y}_t, \mathbf{x}, t)$  corresponds to a full sampling step from  $\mathbf{y}_t$  to  $\mathbf{y}_{t-1}$ , and  $\circ$  denotes the composition of sequential steps.

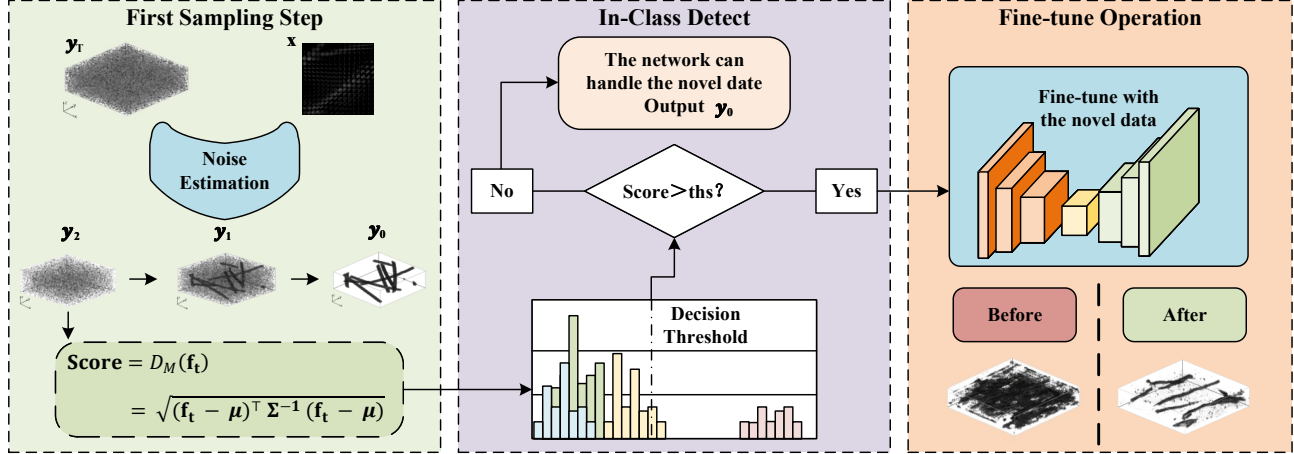


Figure 3. **A schematic overview of the complete workflow incorporating ICD detection.** The figure illustrates how out-of-distribution samples are identified and subsequently handled.

While conventional DDPM frameworks train only the noise estimator  $\epsilon_\theta$ , our model optimizes the entire sampling trajectory by jointly minimizing the reconstruction loss between the final predicted volume and ground truth volumes:

$$\mathcal{L}_{\text{recon}} = \|\mathbf{y}_{\text{gt}} - \mathbf{y}_0\|_2^2, \quad (9)$$

By constructing an end-to-end network, the model can more effectively learn the final reconstruction objective, thereby improving adaptability and performance in high-precision 3D reconstruction tasks.

This unified design bridges probabilistic diffusion with supervised learning, enabling an efficient and task-oriented optimization pipeline that enhances both reconstruction fidelity and computational efficiency.

### 3.2.3. Light-Field-Guided and Lightweight Design

In the TCD model, sequential stacking of multiple U-Net modules causes the network capacity to grow linearly with the number of modules, leading to substantial memory usage and computational overhead. To address this issue, we prune the U-Net backbone, reducing the conventional four-stage architecture to a three-stage design, which significantly reduces the number of parameters and computational cost. However, this reduction in network parameters can weaken its representational capacity, potentially leading to a decrease in reconstruction fidelity.

To compensate for this potential loss and preserve reconstruction fidelity, we introduce a physics-guided conditional prior through a compact Conditional Information Injector. Specifically, the Condition Encoder extracts multi-scale features from the light-field input  $\mathbf{x}$ , which are progressively upsampled, normalized, and averaged to form the condition embedding  $\mathbf{c}_{\text{emb}}$ . This embedding is then fused into the hidden feature map  $\mathbf{h}$  through a lightweight injection oper-

ation:

$$\mathbf{y}_{\text{cond}} = \text{SiLU}(\text{Conv}(\mathbf{h}) + \mathbf{c}_{\text{emb}}), \quad (10)$$

where  $\mathbf{y}_{\text{cond}}$  denotes the fused output.

This design introduces only approximately 0.6 M of additional parameters, thereby compensating for the impact of network pruning. By integrating network pruning with conditional feature injection, we establish an efficient, physics-aware denoising framework that effectively balances reconstruction fidelity and computational cost, as illustrated in Figure 2 and Table 4.

### 3.3. Inter-Class Detection Module

Learning-based LFM volumetric reconstruction methods generally assume that test samples follow a distribution similar to that of the training data. However, in practical microscopy scenarios, variations in imaging conditions—such as optical settings, noise levels, or biological sample types—can significantly degrade generalization and result in unstable reconstruction quality. To address this issue, we propose an Inter-Class Detection module for reliable distribution estimation and adaptive inference during testing.

The ICD module leverages the volume  $\mathbf{y}_{t-1}$  obtained from the first denoising step of the TCD framework. This intermediate volume, which approximately follows a Gaussian distribution and contains reconstructed structural information, is well-suited for distribution modeling. For each training sample, we compute statistical descriptors of the 3D volume, including mean, standard deviation, variance, and L1/L2 norms. These features are aggregated across all training samples and modeled as a multivariate Gaussian distribution to represent the inter-class feature space:

$$p(\mathbf{f}) = \mathcal{N}(\boldsymbol{\mu}, \boldsymbol{\Sigma}), \quad (11)$$

Table 1. **Quantitative comparison with state-of-the-art (SOTA) methods across five representative biological categories.** Bold indicates the best and underline indicates the second-best results.

| Method   | RLD             |                 | VCDNet          |                 | LFMNet          |                 | CWFA            |                 | DDPM            |                 | Ours (TCD)      |                 |
|----------|-----------------|-----------------|-----------------|-----------------|-----------------|-----------------|-----------------|-----------------|-----------------|-----------------|-----------------|-----------------|
| Scene    | PSNR $\uparrow$ | SSIM $\uparrow$ | PSNR $\uparrow$ | SSIM $\uparrow$ | PSNR $\uparrow$ | SSIM $\uparrow$ | PSNR $\uparrow$ | SSIM $\uparrow$ | PSNR $\uparrow$ | SSIM $\uparrow$ | PSNR $\uparrow$ | SSIM $\uparrow$ |
| Tubulin  | 27.60           | 0.749           | 35.58           | <u>0.981</u>    | <u>36.28</u>    | 0.979           | 34.44           | 0.686           | 34.32           | 0.966           | <b>38.41</b>    | <b>0.985</b>    |
| Vessel   | 28.88           | 0.662           | 35.15           | 0.800           | 35.56           | <u>0.814</u>    | <u>35.86</u>    | 0.806           | 30.26           | 0.409           | <b>36.04</b>    | <b>0.825</b>    |
| Bcell    | 37.02           | 0.773           | 40.60           | 0.786           | <u>47.49</u>    | <u>0.972</u>    | 33.63           | 0.629           | 41.03           | 0.875           | <b>47.54</b>    | <b>0.981</b>    |
| Mito     | 42.05           | 0.926           | 35.96           | 0.643           | <u>44.99</u>    | <u>0.949</u>    | 33.19           | 0.679           | 38.20           | 0.889           | <b>45.77</b>    | <b>0.957</b>    |
| Dendrite | 35.59           | 0.724           | 35.58           | 0.570           | <u>37.60</u>    | <u>0.866</u>    | 30.87           | 0.735           | <u>37.79</u>    | 0.808           | <b>38.85</b>    | <b>0.872</b>    |

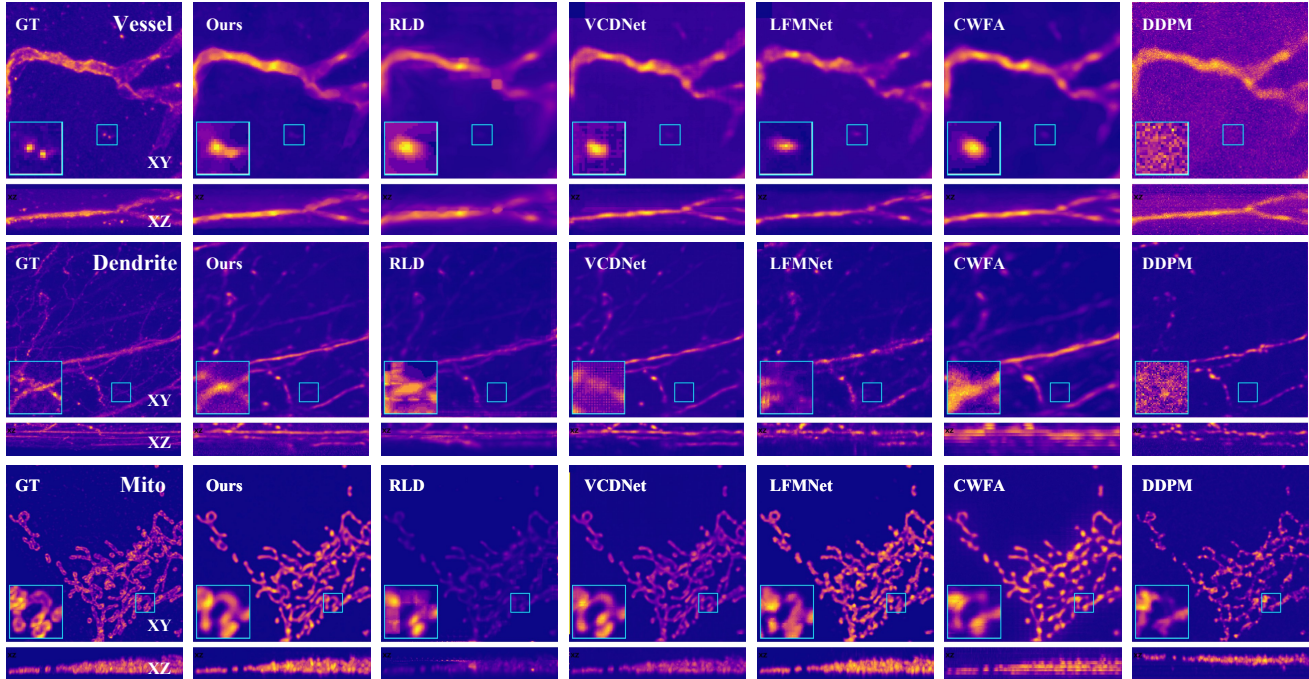


Figure 4. **Qualitative comparisons on the Vessel, Dendrite, and Mito datasets.**

where  $\mu$  and  $\Sigma$  denote the mean vector and covariance matrix of inter-class features, respectively. These parameters are fixed after training and serve as a baseline for anomaly detection during inference.

During testing,  $y_{t-1}$  is extracted for each input sample, and its Mahalanobis distance to the in-distribution (ID) is computed [41]:

$$\text{Score} = D_M(\mathbf{f}_t) = \sqrt{(\mathbf{f}_t - \mu)^\top \Sigma^{-1} (\mathbf{f}_t - \mu)}, \quad (12)$$

where  $\mathbf{f}_t$  denotes the  $t$ -th feature vector. Detection threshold (ths) is determined from the Mahalanobis distance distribution of training samples (e.g., the 85th percentile). Test samples with  $\text{Score} < \text{ths}$  are considered ID and undergo standard TCD reconstruction. Otherwise, they are flagged as potential OOD samples, triggering adaptive strategies such as adding the sample to the training set for fine-tuning or rejecting unreliable outputs.

Experiments show that the module enhances stability for OOD samples, enabling robust volumetric reconstruction across diverse biological specimens.

## 4. Experiments

In this section, we first introduce the experimental setup and datasets for evaluation. Next, we present both quantitative and qualitative comparisons with other SOTA methods. Then, we conduct ablation studies to examine the various components of TCD. Finally, we introduce the ICD module for performance evaluation. For additional experiments, please refer to the supplementary materials.

### 4.1. Experimental Setup and Datasets

We evaluated the performance of the proposed method using both synthetic and real-world biological volumetric data. The experimental dataset consists of five types of 3D volumes, including Tubulin, Vessel, Mito, Dendrite, and

Table 2. Quantitative comparison between models trained on a single dataset (left) and a mixed dataset (right).

| Method   | Train: Dendrite Dataset |                 |                 |                 |                 |                 |                 |                 | Train: Mixed Dataset |                 |                 |                 |                 |                 |                 |                 |
|----------|-------------------------|-----------------|-----------------|-----------------|-----------------|-----------------|-----------------|-----------------|----------------------|-----------------|-----------------|-----------------|-----------------|-----------------|-----------------|-----------------|
|          | Ours (TCD)              |                 | VCDNet          |                 | LFMNet          |                 | DDPM            |                 | Ours (TCD)           |                 | VCDNet          |                 | LFMNet          |                 | DDPM            |                 |
| Scene    | PSNR $\uparrow$         | SSIM $\uparrow$ | PSNR $\uparrow$ | SSIM $\uparrow$ | PSNR $\uparrow$ | SSIM $\uparrow$ | PSNR $\uparrow$ | SSIM $\uparrow$ | PSNR $\uparrow$      | SSIM $\uparrow$ | PSNR $\uparrow$ | SSIM $\uparrow$ | PSNR $\uparrow$ | SSIM $\uparrow$ | PSNR $\uparrow$ | SSIM $\uparrow$ |
| Bcell    | <b>37.15</b>            | <b>0.885</b>    | 34.41           | 0.693           | <u>37.02</u>    | <u>0.841</u>    | 32.99           | 0.751           | <b>39.822</b>        | <b>0.926</b>    | 37.647          | 0.820           | <u>39.368</u>   | <u>0.922</u>    | 33.061          | 0.758           |
| Dendrite | <b>38.85</b>            | <b>0.872</b>    | 35.58           | 0.570           | <u>37.60</u>    | <u>0.866</u>    | <u>37.79</u>    | 0.808           | <b>37.287</b>        | <b>0.834</b>    | <u>34.629</u>   | <u>0.773</u>    | <u>34.455</u>   | 0.730           | 33.211          | 0.654           |
| Mito     | <u>34.51</u>            | <u>0.816</u>    | 31.87           | 0.316           | <b>36.95</b>    | <b>0.899</b>    | 31.25           | 0.583           | <b>41.346</b>        | <b>0.935</b>    | 35.883          | 0.649           | <u>38.459</u>   | <u>0.916</u>    | 32.521          | 0.633           |
| Vessel   | <u>31.43</u>            | <u>0.647</u>    | <b>32.91</b>    | <b>0.657</b>    | 29.75           | 0.642           | 28.98           | 0.479           | <b>33.230</b>        | <b>0.728</b>    | 31.734          | 0.589           | <u>32.672</u>   | <u>0.717</u>    | 29.507          | 0.500           |
| Tubulin  | 27.69                   | <u>0.640</u>    | <b>30.54</b>    | 0.354           | <u>28.49</u>    | <b>0.794</b>    | 26.86           | 0.523           | <b>37.861</b>        | <b>0.965</b>    | 33.977          | 0.690           | <u>34.542</u>   | <u>0.938</u>    | 30.098          | 0.631           |

Table 3. Efficiency comparison with SOTA methods.

| Method     | PSNR $\uparrow$ | SSIM $\uparrow$ | Train. (h) | Param. (M) | Inf. (s) |
|------------|-----------------|-----------------|------------|------------|----------|
| RLD        | 34.63           | 0.767           | —          | —          | 194.991  |
| VCDNet     | 36.17           | 0.756           | 2.0        | 18.8       | 0.042    |
| LFMNet     | 40.38           | 0.916           | 2.0        | 22.0       | 0.021    |
| CWFA       | 33.20           | 0.707           | 2.6        | 43.5       | 0.214    |
| DDPM       | 36.32           | 0.789           | 2.2        | 37.9       | 4.256    |
| Ours (TCD) | 41.72           | 0.924           | 2.6        | 32.5       | 0.062    |

Bead cell (Bcell). First, the original volumetric data were cropped and resampled to achieve a uniform resolution and remove redundant edge information, yielding standardized 3D volumes. Subsequently, these volumes were projected into light-field images using a physics-based forward projection method, simulating the acquisition of light-field information in practical microscopy. To ensure representative testing, we selected five typical cases from the dataset as the test set, covering different biological structures.

All experiments were conducted on an NVIDIA RTX 3090 GPU to handle the computational demands of large-scale volumetric data. In each experiment, reconstruction quality was quantitatively evaluated using metrics such as PSNR and SSIM, validating the performance of all methods across diverse biological structures and imaging conditions.

## 4.2. Comparative Experiments

We performed a comprehensive quantitative comparison between the proposed method and several representative state-of-the-art LFM 3D reconstruction approaches, including the traditional algorithm-based Richardson–Lucy deconvolution (RLD, 8 iterations) [3], the convolutional neural network-based VCDNet [39], the four-dimensional convolution model LFMNet [38], the invertible wavelet flow model (CWFA) [22], and our baseline diffusion-based model (DDPM) [12]. All methods were trained and evaluated under identical experimental settings to ensure a fair comparison.

As shown in Table 1, we report the quantitative metrics for each model trained and tested on its corresponding dataset. The reconstructed results and the ground-truth 3D volumes (GT) in the XY and XZ central planes are further illustrated in Figure 4. The results demonstrate that the pro-

posed TCD framework consistently achieves the best performance across all tested scenes, significantly outperforming other methods in detail restoration and exhibiting superior spatial fidelity.

The cross-sample evaluation results obtained when models are trained on the dendrite dataset (left), as well as the overall performance on a mixed dataset comprising five biological categories (right), are presented in Table 2. The results show that TCD achieves optimal or sub-optimal performance in cross-sample testing under single-sample training conditions, and significantly outperforms other methods when trained and tested on multi-category samples. These findings demonstrate the strong generalization and robustness capability of TCD. Furthermore, the supplementary materials provide visual comparisons of reconstruction results between TCD and other methods after training on the mixed dataset, further demonstrating its superiority in detail and structural reconstruction.

A comprehensive comparison of all methods in terms of model complexity and computational efficiency is provided in Table 3, including PSNR, SSIM (averaged results from Table 1), training time ( $\downarrow$ ), parameter count ( $\downarrow$ ), and inference time ( $\downarrow$ ). The results show that TCD offers significant advantages in computational efficiency compared with traditional algorithm-based approaches and the DDPM model.

## 4.3. Ablation Experiments

The ablation experiments were conducted on the Tubulin dataset. As shown in Figure 5, we evaluated the impact of the sampling step  $T$  on reconstruction quality and computational cost, including PSNR ( $\uparrow$ ), SSIM ( $\uparrow$ ), LPIPS ( $\downarrow$ , learned perceptual image patch similarity), EPI ( $\uparrow$ , edge preservation index), training time ( $\downarrow$ , h), GPU memory consumption ( $\downarrow$ , GB), parameter count ( $\downarrow$ , M), and inference time ( $\downarrow$ , s). The results indicate that when  $T < 3$ , the reconstruction performance increases significantly, while for  $T > 3$ , the performance gain tends to saturate. Meanwhile, the computational cost grows approximately linearly. Therefore, we select  $T = 3$  as the optimal trade-off between quality and computational efficiency.

As shown in Table 4, we conducted systematic ablation studies on the key components of the TCD framework, including the sampling steps  $T$ , end-to-end training (E2E),

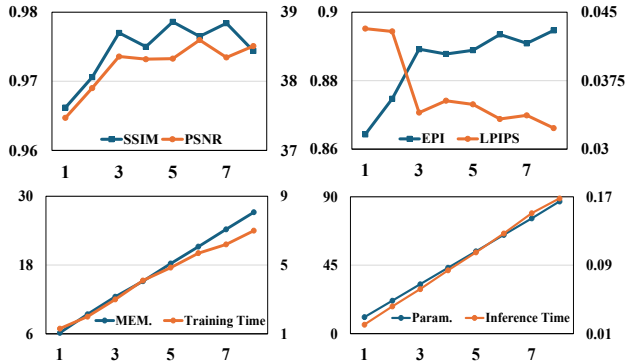


Figure 5. Comparison of TCD model variants with varying step  $1 \leq T \leq 8$ .

Table 4. Ablation study of TCD under different configurations.

| Method | $T$ | E2E | Inj. | Pru. | PSNR         | SSIM         | EPI          | LPIPS        | Inf.         | Param.      |
|--------|-----|-----|------|------|--------------|--------------|--------------|--------------|--------------|-------------|
| DDPM   | 300 | ×   | ×    | ×    | 33.02        | 0.954        | 0.617        | 0.123        | 3.080        | 37.9        |
| DDPM   | 500 | ×   | ×    | ×    | 33.65        | 0.961        | 0.673        | 0.097        | 5.101        | 37.9        |
| DDPM   | 700 | ×   | ×    | ×    | 33.24        | 0.958        | 0.607        | 0.117        | 6.960        | 37.9        |
| DDIM   | 50  | ×   | ×    | ×    | 33.17        | 0.957        | 0.649        | 0.104        | 0.552        | 37.9        |
| Ours   | 3   | ✓   | ×    | ×    | 37.86        | <u>0.971</u> | 0.879        | 0.040        | 0.076        | 114.5       |
| Ours   | 3   | ✓   | ×    | ✓    | 37.64        | 0.963        | 0.865        | 0.047        | <b>0.062</b> | <b>31.9</b> |
| Ours   | 3   | ✓   | ✓    | ×    | <b>38.46</b> | <b>0.985</b> | <b>0.893</b> | <b>0.032</b> | 0.075        | 115.7       |
| Ours   | 3   | ✓   | ✓    | ✓    | <u>38.41</u> | <b>0.985</b> | <u>0.892</u> | <b>0.032</b> | <b>0.062</b> | <u>32.5</u> |

conditional information injector (Inj.), and U-Net pruning (Pru.), to investigate their effects on model performance. The evaluation metrics include PSNR ( $\uparrow$ ), SSIM ( $\uparrow$ ), EPI ( $\uparrow$ ), Inf. ( $\downarrow$ , s), and Param. ( $\downarrow$ , M). The experimental results demonstrate that the end-to-end TCD significantly outperforms DDPM and DDIM in reconstruction quality, while reducing the required sampling steps by over 90% compared to DDPM. This reduction leads to a two-order-of-magnitude acceleration in inference speed. Although pruning the U-Net slightly decreases reconstruction accuracy, it reduces model parameters by approximately 70%, substantially lowering GPU memory consumption. Moreover, introducing the conditional information injector compensates for the performance degradation caused by pruning, achieving an optimal balance between accuracy and efficiency.

#### 4.4. Inter-Class Detection for Sample Adaptation

To further enhance the model’s generalization capability across different biological categories, we evaluated the integrated ICD module. As illustrated in Figure 6, we designate Bcell as the ID category and construct a mixed test set containing five biological structures to assess the recognition performance of TCD+ICD and LFMNet+ICD. In the figure, the vertical axis denotes the biological category of each test sample, while the horizontal axis represents the Score computed by the ICD module. A lower Score indicates a higher similarity between the test and ID samples, and samples with Scores below a predefined threshold are classified

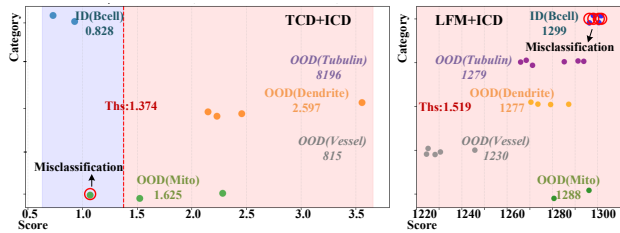


Figure 6. Framework comparison between TCD+ICD (left) and LFMNet+ICD (right).

as ID samples.

Experimental results demonstrate that TCD+ICD effectively distinguishes most ID and OOD samples, whereas LFMNet+ICD fails to achieve stable recognition performance, showing difficulty in separating these categories. This finding further verifies the high compatibility and synergy between the ICD module and the proposed TCD framework.

Furthermore, we conducted targeted fine-tuning experiments on the detected OOD samples (see supplementary material for details). The results show that, compared with training from scratch, the ICD-guided fine-tuning process reduces the time required to reach a loss of  $10^{-3}$  by approximately half, significantly improving the model’s adaptation efficiency. Notably, as shown in Figure 6, although a few OOD samples are misclassified as ID samples due to their structural similarity, TCD still maintains robust reconstruction performance and effectively generates valid 3D volumes, benefiting from its superior cross-sample generalization capability.

## 5. Limitations and Future Work

In this study, we proposed a high-efficiency, end-to-end diffusion-based 3D reconstruction method for LFM, termed TCD, which is built upon a lightweight conditional U-Net architecture. Our method achieves high-accuracy 3D imaging while significantly improving inference efficiency, offering a pioneering solution for efficient and high-fidelity LFM reconstruction. However, the current ICD module is not yet widely applicable to other models, and a more generalized reconstruction pipeline has yet to be established.

Although the proposed TCD+ICD framework demonstrates superior performance in LFM 3D reconstruction and exhibits strong cross-sample generalization capability, two directions remain open for further exploration: (1) optimizing macroscopic structure reconstruction to enhance adaptability to large-scale biological samples; (2) incorporating physical model constraints, such as PSF modeling or optical prior refinement, during training to further improve reconstruction accuracy and robustness under unsupervised or weakly supervised conditions.

## Acknowledgments

This work was supported by Hebei Natural Science Foundation (No. F2024203081), National Natural Science Foundation of China (No. 62371006), and Beijing Natural Science Foundation (No. 3242008).

## References

- [1] Sophie Aimon, Takeo Katsuki, Tongqiu Jia, Logan Grosenick, Michael Broxton, Karl Deisseroth, Terrence J Sejnowski, and Ralph J Greenspan. Fast near-whole-brain imaging in adult drosophila during responses to stimuli and behavior. *PLoS biology*, 17(2):e2006732, 2019. 2
- [2] Tom E Bishop and Paolo Favaro. The light field camera: Extended depth of field, aliasing, and superresolution. *IEEE transactions on pattern analysis and machine intelligence*, 34(5):972–986, 2011. 2
- [3] Michael Broxton, Logan Grosenick, Samuel Yang, Noy Cohen, Aaron Andalman, Karl Deisseroth, and Marc Levoy. Wave optics theory and 3-d deconvolution for the light field microscope. *Optics express*, 21(21):25418–25439, 2013. 1, 2, 7
- [4] Bin Chen, Zhenyu Zhang, Weiqi Li, Chen Zhao, Jiwen Yu, Shijie Zhao, Jie Chen, and Jian Zhang. Invertible diffusion models for compressed sensing. *IEEE Transactions on Pattern Analysis and Machine Intelligence*, 2025. 2
- [5] Jiji Chen, Hideki Sasaki, Hoyin Lai, Yijun Su, Jiamin Liu, Yicong Wu, Alexander Zhovmer, Christian A Combs, Ivan Rey-Suarez, Hung-Yu Chang, et al. Three-dimensional residual channel attention networks denoise and sharpen fluorescence microscopy image volumes. *Nature methods*, 18(6):678–687, 2021. 2
- [6] Minshuo Chen, Song Mei, Jianqing Fan, and Mengdi Wang. Opportunities and challenges of diffusion models for generative ai. *National Science Review*, 11(12):nwae348, 2024. 3
- [7] Yanqin Chen, Xin Jin, and Bo Xiong. Optical-aberrations-corrected light field re-projection for high-quality plenoptic imaging. *Optics Express*, 28(3):3057–3072, 2020. 2
- [8] Lin Cong, Zeguan Wang, Yuming Chai, Wei Hang, Chunfeng Shang, Wenbin Yang, Lu Bai, Jiulin Du, Kai Wang, and Quan Wen. Rapid whole brain imaging of neural activity in freely behaving larval zebrafish (*danio rerio*). *elife*, 6:e28158, 2017. 1
- [9] Prafulla Dhariwal and Alexander Nichol. Diffusion models beat gans on image synthesis. *Advances in neural information processing systems*, 34:8780–8794, 2021. 3
- [10] Nicolas Dufour, Victor Besnier, Vicky Kalogeiton, and David Picard. Don’t drop your samples! coherence-aware training benefits conditional diffusion. In *Proceedings of the IEEE/CVF Conference on Computer Vision and Pattern Recognition*, pages 6264–6273, 2024. 3
- [11] Kyungpil Gwon and Joonhyuk Yoo. Out-of-distribution (ood) detection and generalization improved by augmenting adversarial mixup samples. *Electronics*, 12(6):1421, 2023. 2
- [12] Jonathan Ho, Ajay Jain, and Pieter Abbeel. Denoising diffusion probabilistic models. *Advances in neural information processing systems*, 33:6840–6851, 2020. 2, 3, 7
- [13] Kimin Lee, Kibok Lee, Honglak Lee, and Jinwoo Shin. A simple unified framework for detecting out-of-distribution samples and adversarial attacks. *Advances in neural information processing systems*, 31, 2018. 3
- [14] Marc Levoy, Ren Ng, Andrew Adams, Matthew Footer, and Mark Horowitz. Light field microscopy. In *Acm siggraph 2006 papers*, pages 924–934. 2006. 2
- [15] Marc Levoy, Zhengyun Zhang, and Ian McDowall. Recording and controlling the 4d light field in a microscope using microlens arrays. *Journal of microscopy*, 235(2):144–162, 2009. 2
- [16] Senmao Li, Taihang Hu, Joost van de Weijer, Fahad S Khan, Tao Liu, Linxuan Li, Shiqi Yang, Yaxing Wang, Ming-Ming Cheng, and Jian Yang. Faster diffusion: Rethinking the role of the encoder for diffusion model inference. *Advances in Neural Information Processing Systems*, 37:85203–85240, 2024. 2
- [17] Yue Li, Yijun Su, Min Guo, Xiaofei Han, Jiamin Liu, Harshad D Vishwasrao, Xuesong Li, Ryan Christensen, Titas Sengupta, Mark W Moyle, et al. Incorporating the image formation process into deep learning improves network performance. *Nature Methods*, 19(11):1427–1437, 2022. 2
- [18] Shiyu Liang, Yixuan Li, and Rayadurgam Srikant. Enhancing the reliability of out-of-distribution image detection in neural networks. *arXiv preprint arXiv:1706.02690*, 2017. 3
- [19] Jiawei Liu, Qiang Wang, Huijie Fan, Yinong Wang, Yandong Tang, and Liangqiong Qu. Residual denoising diffusion models. In *Proceedings of the IEEE/CVF Conference on Computer Vision and Pattern Recognition*, pages 2773–2783, 2024. 2, 3
- [20] Zhi Lu, Jiamin Wu, Hui Qiao, You Zhou, Tao Yan, Zijing Zhou, Xu Zhang, Jingtao Fan, and Qionghai Dai. Phase-space deconvolution for light field microscopy. *Optics express*, 27(13):18131–18145, 2019. 2
- [21] Haomiao Ni, Changhao Shi, Kai Li, Sharon X Huang, and Martin Renqiang Min. Conditional image-to-video generation with latent flow diffusion models. In *Proceedings of the IEEE/CVF Conference on Computer Vision and Pattern Recognition*, pages 18444–18455, 2023. 3
- [22] Josué Page Vizcaíno, Panagiotis Symvoulidis, Zeguan Wang, Jonas Jelten, Paolo Favaro, Edward S Boyden, and Tobias Lasser. Fast light-field 3d microscopy with out-of-distribution detection and adaptation through conditional normalizing flows. *Biomedical Optics Express*, 15(2):1219–1232, 2024. 2, 7
- [23] Robert Prevedel, Young-Gyu Yoon, Maximilian Hoffmann, Nikita Pak, Gordon Wetzstein, Saul Kato, Tina Schrödel, Ramesh Raskar, Manuel Zimmer, Edward S Boyden, et al. Simultaneous whole-animal 3d imaging of neuronal activity using light-field microscopy. *Nature methods*, 11(7):727–730, 2014. 2
- [24] Bohan Qu, Zhouyu Jin, You Zhou, Bo Xiong, and Xun Cao. Deep-learning-based noise correction method for light-field fluorescence microscopy. *Photonics Research*, 13(9):2547–2565, 2025. 1

- [25] Robin Rombach, Andreas Blattmann, Dominik Lorenz, Patrick Esser, and Björn Ommer. High-resolution image synthesis with latent diffusion models. In *Proceedings of the IEEE/CVF conference on computer vision and pattern recognition*, pages 10684–10695, 2022. 3
- [26] Ludan Ruan, Yiyang Ma, Huan Yang, Huiguo He, Bei Liu, Jianlong Fu, Nicholas Jing Yuan, Qin Jin, and Baining Guo. Mm-diffusion: Learning multi-modal diffusion models for joint audio and video generation. In *Proceedings of the IEEE/CVF Conference on Computer Vision and Pattern Recognition*, pages 10219–10228, 2023. 3
- [27] Chitwan Saharia, William Chan, Saurabh Saxena, Lala Li, Jay Whang, Emily L Denton, Kamyar Ghasemipour, Raphael Gontijo Lopes, Burcu Karagol Ayan, Tim Salimans, et al. Photorealistic text-to-image diffusion models with deep language understanding. *Advances in neural information processing systems*, 35:36479–36494, 2022. 3
- [28] Simon R Schultz, Caroline S Copeland, Amanda J Foust, Peter Quicke, and Renaud Schuck. Advances in two-photon scanning and scanless microscopy technologies for functional neural circuit imaging. *Proceedings of the IEEE*, 105(1):139–157, 2016. 2
- [29] Sapna A Shroff and Kathrin Berkner. Image formation analysis and high resolution image reconstruction for plenoptic imaging systems. *Applied optics*, 52(10):D22–D31, 2013. 1, 2
- [30] Jascha Sohl-Dickstein, Eric Weiss, Niru Maheswaranathan, and Surya Ganguli. Deep unsupervised learning using nonequilibrium thermodynamics. In *International conference on machine learning*, pages 2256–2265. pmlr, 2015. 3
- [31] Yang Song, Jascha Sohl-Dickstein, Diederik P Kingma, Abhishek Kumar, Stefano Ermon, and Ben Poole. Score-based generative modeling through stochastic differential equations. *arXiv preprint arXiv:2011.13456*, 2020. 3
- [32] Anca Stefanoiu, Josue Page, Panagiotis Symvoulidis, Gil G Westmeyer, and Tobias Lasser. Artifact-free deconvolution in light field microscopy. *Optics express*, 27(22):31644–31666, 2019. 2
- [33] Anca Stefanoiu, Gabriele Scrofani, Genaro Saavedra, Manuel Martínez-Corral, and Tobias Lasser. 3d deconvolution in fourier integral microscopy. In *Computational Imaging V*, pages 56–63. SPIE, 2020. 2
- [34] Changqing Su, Yuhan Gao, You Zhou, Yaoqi Sun, Chenggang Yan, Haibing Yin, and Bo Xiong. Autodeconj: a gpu-accelerated imagej plugin for 3d light-field deconvolution with optimal iteration numbers predicting. *Bioinformatics*, 39(1):btac760, 2023. 2
- [35] Vaiva Vasiliauskaite and Nino Antulov-Fantulin. Generalization of neural network models for complex network dynamics. *Communications Physics*, 7(1):348, 2024. 3
- [36] Herman Verinaz-Jadan, Pingfan Song, Carmel L Howe, Amanda J Foust, and Pier Luigi Dragotti. Volume reconstruction for light field microscopy. In *ICASSP 2020-2020 IEEE International Conference on Acoustics, Speech and Signal Processing (ICASSP)*, pages 1459–1463. IEEE, 2020. 1, 2
- [37] Herman Verinaz-Jadan, Pingfan Song, Carmel L Howe, Amanda J Foust, and Pier Luigi Dragotti. Shift-invariant subspace discretization and volume reconstruction for light field microscopy. *IEEE Transactions on Computational Imaging*, 8:286–301, 2022. 1, 2
- [38] Josue Page Vizcaino, Federico Saltarin, Yury Belyaev, Ruth Lyck, Tobias Lasser, and Paolo Favaro. Learning to reconstruct confocal microscopy stacks from single light field images. *IEEE transactions on computational imaging*, 7:775–788, 2021. 2, 7
- [39] Zhaoqiang Wang, Lanxin Zhu, Hao Zhang, Guo Li, Chengqiang Yi, Yi Li, Yicong Yang, Yichen Ding, Mei Zhen, Shangbang Gao, et al. Real-time volumetric reconstruction of biological dynamics with light-field microscopy and deep learning. *Nature methods*, 18(5):551–556, 2021. 2, 7
- [40] Chenyu Xu, Zhouyu Jin, Chengkang Shen, Hao Zhu, Zhan Ma, Bo Xiong, You Zhou, Xun Cao, and Ning Gu. 3d gaussian adaptive reconstruction for fourier light-field microscopy. *arXiv preprint arXiv:2505.12875*, 2025. 1
- [41] Donghun Yang, Iksoo Shin, Mai Ngoc Kien, Hoyong Kim, Chanhee Yu, and Myunggwon Hwang. Out-of-distribution detection based on distance metric learning. In *The 9th International Conference on Smart Media and Applications*, pages 214–218, 2020. 3, 6
- [42] Chengqiang Yi, Lanxin Zhu, Dongyu Li, and Peng Fei. Light field microscopy in biological imaging. *Journal of Innovative Optical Health Sciences*, 16(01):2230017, 2023. 1
- [43] Lvmin Zhang, Anyi Rao, and Maneesh Agrawala. Adding conditional control to text-to-image diffusion models. In *Proceedings of the IEEE/CVF international conference on computer vision*, pages 3836–3847, 2023. 3
- [44] Jiayin Zhao, Zhenqi Fu, Tao Yu, and Hui Qiao. V2v3d: View-to-view denoised 3d reconstruction for light field microscopy. In *Proceedings of the Computer Vision and Pattern Recognition Conference*, pages 26451–26461, 2025. 2, 3
- [45] Weisong Zhao, Shiqun Zhao, Liuju Li, Xiaoshuai Huang, Shijia Xing, Yulin Zhang, Guohua Qiu, Zhenqian Han, Yingxu Shang, De-en Sun, et al. Sparse deconvolution improves the resolution of live-cell super-resolution fluorescence microscopy. *Nature biotechnology*, 40(4):606–617, 2022. 2
- [46] You Zhou, Zhouyu Jin, Qianhui Zhao, Bo Xiong, and Xun Cao. Aberration modeling in deep learning for volumetric reconstruction of light-field microscopy. *Laser & Photonics Reviews*, 17(10):2300154, 2023. 1
- [47] Hao Zhu, Shaowen Xie, Zhen Liu, Fengyi Liu, Qi Zhang, You Zhou, Yi Lin, Zhan Ma, and Xun Cao. Disorder-invariant implicit neural representation. *IEEE Transactions on Pattern Analysis and Machine Intelligence*, 46(8):5463–5478, 2024. 2